AGU ADVANCING EARTH AND SPACE SCIENCES

Geophysical Research Letters

RESEARCH LETTER
10.1029/2025GL118496

Quantifying the Influence of Climate on Storm Activity Using Machine Learning

Or Hadas[1] and **Yohai Kaspi**[1]

[1]Department of Earth and Planetary Sciences, Weizmann Institute of Science, Rehovot, Israel

Key Points:

- Using 84 years of ERA-5 reanalysis and thousands of storm tracks, a machine-learning approach quantifies how climate shapes storm activity
- Climatic forcing accounts for only a third of individual storm variability, while it does account for over 90% of average storm activity
- Thus, attribution efforts should focus on a climatic perspective or on factors directly connected to anthropogenic climate change

Supporting Information:

Supporting Information may be found in the online version of this article.

Correspondence to:

O. Hadas,
or.hadas@weizmann.ac.il

Citation:

Hadas, O., & Kaspi, Y. (2026). Quantifying the influence of climate on storm activity using machine learning. *Geophysical Research Letters*, *53*, e2025GL118496. https://doi.org/10.1029/2025GL118496

Received 28 MAY 2025
Accepted 23 DEC 2025

Author Contributions:

Conceptualization: Or Hadas, Yohai Kaspi
Formal analysis: Or Hadas
Funding acquisition: Yohai Kaspi
Investigation: Or Hadas
Methodology: Or Hadas
Software: Or Hadas
Supervision: Yohai Kaspi
Visualization: Or Hadas
Writing – original draft: Or Hadas
Writing – review & editing: Yohai Kaspi

Abstract Midlatitude storms vary due to the slowly evolving climate and the rapidly changing synoptic conditions. While the impact of both factors has been studied extensively, their relative contributions remain poorly quantified. We use 84 years of ERA-5 reanalysis data and convolutional neural networks to assess the relative importance of seasonal climatology versus synoptic conditions in controlling averaged and individual storm activity. Our models successfully predict over 90% of the variability in mean storm activity, showing climatic conditions dominate it. However, only one-third of the variability in individual storm properties is attributed to climatic factors, indicating that synoptic conditions dominate individual storm characteristics. Further isolating the impact of long-term climate trends on individual storms shows that it contributes to storm-intensity variability only $0.36(\pm 0.08)\frac{\%}{C^\circ}$. In contrast, its contribution to storms' associated heat anomalies is over three times greater, demonstrating that variables directly linked to global warming provide a clearer pathway for weather attribution.

Plain Language Summary Extratropical storms, which play a major role in shaping midlatitude weather, are influenced by both long-term climate patterns and short-term atmospheric variability. In this study, 84 years of atmospheric data combined with machine learning techniques are used to quantify the extent to which seasonal climate shapes storm activity. The results show that long-term averaged storm activity is strongly tied to the climate, whereas the behavior of individual storms, including their maximum intensity and path, is largely governed by short-term and small-scale variations. When measuring the impact of recent climate change on individual storms, the signal is extremely weak compared to the background of natural variability. In contrast, the climate change signal is clearer for warm temperature anomalies associated with storms. These findings suggest that attributing specific midlatitude weather events to climate change is extremely challenging, and that efforts should focus on factors that are more directly linked to long-term climate trends.

1. Introduction

When attempting to attribute extreme extratropical weather events, often associated with cyclones and anticyclones, to changes in Climatic Forcing (CF) (Ginesta et al., 2023; Philip et al., 2022), a major uncertainty arises from the Synoptic Variability (SV) of storms. Over extended periods, the averaged atmospheric flow is expected to be influenced primarily by CF, such as solar insolation, sea surface temperature anomalies, and the greenhouse effect. However, due to the chaotic nature of weather, the dynamics of individual storms exhibit large SV, which results from the fine structure of the meteorological conditions during their formation. Although SV and CF play significant roles in determining the intensity and trajectory of individual storms, their relative importance has yet to be fully quantified. Bridging this knowledge gap can uncover the importance of the dynamical response of storms to changes in CF when studying individual weather events. Therefore, in this study, using a statistical approach, we attempt to quantify the importance of CF to the growth of individual storms and the seasonally averaged storm activity.

The effect of CF on midlatitude climate and weather has traditionally been studied by decomposing the flow into a mean (spatially or temporally averaged) and an eddy component. Within this framework, the mean flow primarily reflects climatological features, such as the jet stream, while eddies describe synoptic-scale weather systems. Hence, given a particular CF, serving as a boundary condition, one expects a characteristic midlatitude flow pattern, consisting of a mean flow and a spectrum of eddies. Our central goal is to quantify how strongly these synoptic eddies (storms) are connected to the mean flow, both in the time-averaged sense (seasonal storm activity) and at the scale of individual storm growth.

The interaction between the mean flow and midlatitude storms is well studied, both from theoretical and idealized perspectives (Charney, 1947; Eady, 1949; Harnik & Chang, 2004; Phillips, 1954), as well as in relation to the seasonal alternation in the intensity of the storm tracks (Nakamura, 1992; Schemm & Rivière, 2019), and the effect on individual storms (Hadas & Kaspi, 2025; Hadas et al., 2023; Orlanski & Chang, 1993; Orlanski & Katzfey, 1991; Rivière & Joly, 2006; Schemm et al., 2020). Despite this extensive literature, the fundamental question of the degree to which the mean flow dictates the characteristics of individual storms has not been addressed quantitatively.

In this study, we use 84 years of ERA-5 reanalysis (Section 2.1) and tracks of about 100,000 cyclones and 50,000 anticyclones (Section 2.2) to quantify the extent to which storm activity is consistent with the mean flow from a statistical perspective. To investigate this relationship, we use two modeling approaches. First, the climatic model (Section 2.3) tests whether the link between the mean flow and the seasonal storm activity is unique (Section 3.1). Second, the single storm model (Section 2.4) evaluates how strongly the mean flow influences the properties of individual storms (Section 3.2). Finally, we discuss the implications of our findings for the attribution of weather events to current anthropogenic climate change (Section 3.3).

2. Methods

2.1. Reanalysis Data

Data from the ERA-5 reanalysis by the European Centre for Medium-Range Weather Forecasts (Hersbach et al., 2020; Soci et al., 2024), spanning from 1940 to 2023, is employed for current climate assessment. The ERA-5 reanalysis provides estimates of atmospheric variables with a horizontal resolution of 31 km and 137 vertical levels. Three-hourly Sea Level Pressure (SLP) data is utilized to track cyclones and anticyclones, while 3-hourly temperature (T), specific humidity (Q), zonal wind (U), and meridional wind (V) at pressure levels 300, 500, and 850 hPa are utilized to estimate the atmospheric state and its climatology. Discarding the backward extension (1940–1978) results in slightly (1%–2%) higher model performance.

The global mean surface temperature difference between 1980 and 2023 was estimated by fitting a linear trend to annual global mean surface temperature data from the GISS Surface Temperature Analysis version 4 (Lenssen et al., 2024) and comparing the fitted values for these two years. The uncertainty was calculated as the 90% confidence interval of the slope's standard error multiplied by the time span (43 years). The resulting estimate is $\Delta T = 0.86(\pm 0.14)\,\mathrm{C}^{\circ}$.

2.2. Storm Tracking

A feature point tracking algorithm (Hodges, 1995; Tamarin & Kaspi, 2016, 2017a, 2017b) is applied to SLP data to identify and characterize extratropical cyclones and anticyclones. To reduce noise, the data is smoothed to a T63 resolution. The background, defined as zonal wavenumbers $0-4$, is removed to isolate the synoptic scale dynamics. Only SLP anomalies deeper than 8 hPa are tracked to focus on significant events. After identification, systems are tracked, and their location and intensity are recorded if they persist for more than 48 hr and move more than 500 km eastward. Additionally, systems that reach peak intensity over topography higher than 1 km are filtered out.

The tracking algorithm returns the positions and depth (in hPa) of the storms from genesis to lysis. The output of the tracking algorithm is used to quantify the growth of storms using four metrics: the maximum intensity, defined as the maximum depth of the storm normalized by the sinus of latitude (Sanders & Gyakum, 1980), the growth time, defined as the time between identification and maximum intensity, and the meridional and zonal rate of propagation of the storm from genesis to maximum intensity. In addition, the maximum 850 hPa temperature anomaly associated with a cyclone is defined as the maximum temperature anomaly around the cyclone center in a composite of $15^{\circ}\pm$ in the zonal direction and $10^{\circ}\pm$ in the meridional direction. An anomaly is defined as the deviation from the 84-year grid and time of the year average.

2.3. Climatic Model

The connection between the mean flow and seasonal storm activity is treated as an image-to-image regression problem (Figure 1), solved using Convolutional Neural Network (CNN), due to its ability to efficiently learn spatial hierarchies and patterns in structured data. The model input is the three-dimensional distribution of $\overline{U}$, $\overline{V}$,

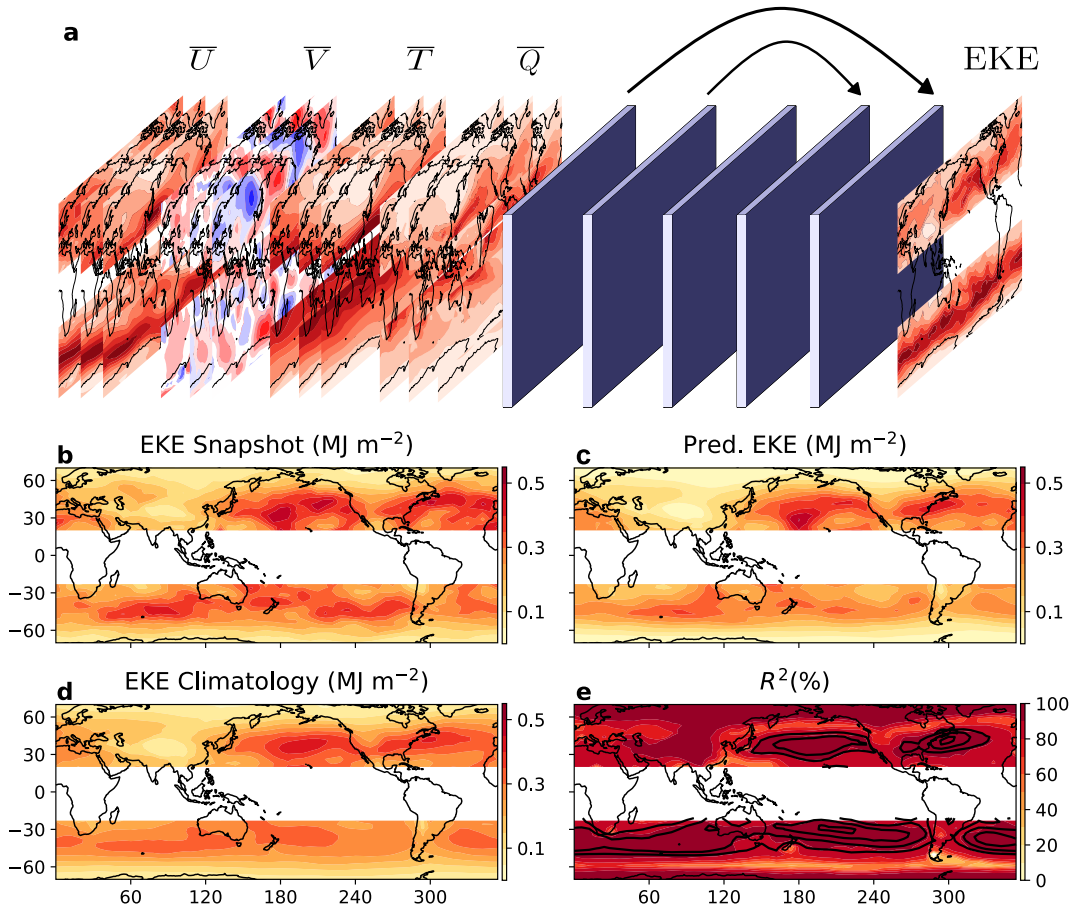

Figure 1. (a) Illustration of the climatic model. (b–d) An EKE example snapshot centered on 17 of 20 November 2012, the model prediction for the snapshot, and the climatology of data points centered in November (MJ m^{-2}, computed using Equation 1). (e) R^2 score, calculated over the test set (shading), and the multi-annual mean EKE, depicted as contours ranging from 0.18 to 0.38 (MJ m^{-2}) in intervals of 0.02.

$\overline{Q}$, and $\overline{T}$ over the midlatitudes (latitudes 20° − 80° in both hemispheres), where the bar represents a 90-day moving mean (45 days in each direction), which is a commonly used timescale for examining the relationship between the seasonal mean atmospheric state and storm activity. The output is the distribution of vertically integrated Eddy Kinetic Energy (EKE) over the midlatitudes (latitudes 20° − 80° in both hemispheres):

$$\mathrm{EKE} = \frac{1}{2g}\int_{850}^{300} \overline{u'^2 + v'^2}\, dp, \tag{1}$$

where the bar is defined the same as above, the prime is defined as a deviation from a 10-day moving mean to focus on synoptic activity, and the integration is performed between 300 and 850 hPa. The data is temporarily split into training (50%), validation (20%), and test (30%) sets. An in-depth discussion of the data appears in Section S1 in Supporting Information S1.

Averaging the data over time substantially simplifies the regression task by reducing the effective image size in the frequency domain. Because atmospheric waves typically follow a dispersion relation, where lower frequency waves tend to be larger, this temporal averaging further diminishes the impact of small-scale waves on variability (Figures S1a–S1c in Supporting Information S1). This simplification achieved can be quantified by the number of principal components required to capture 90% of the variability in the data set. Analyzing this reveals that filtering reduces the number of required components by 80% (Figure S1d in Supporting Information S1). In addition, time averaging significantly simplifies the dynamics, as it nullifies (or at least significantly reduces) the

contribution of many physical processes to the overall system (Vallis, 2017). Consequently, much simpler models can simulate the relation between mean and eddy flow, relative to numerical weather prediction models (Bi et al., 2023; Kochkov et al., 2024; Lam et al., 2023).

The model is built out of a series of convolutional layers (Guan et al., 2023; Krizhevsky et al., 2012). Given an input, it predicts the shape and scale parameters of the underlying Gamma distribution, which are optimized using negative log-likelihood loss (Equation S2 in Supporting Information S1), similar to Guillaumin and Zanna (2021). An in-depth discussion of the model, including the loss function, structure, hyperparameters, and steps taken to avoid overfitting, is provided in Section S2 in Supporting Information S1.

2.4. Single Storm Model

The extent to which the mean flow sets the growth of individual storms is tested by constructing a model that predicts the average outcome of a storm's growth based on the mean flow it experiences at genesis. The model input is the three-dimensional composites of $\overline{U}$, $\overline{V}$, $\overline{Q}$, and $\overline{T}$ around the storm at genesis, where mean is defined as in Section 2.3. The model output is the outcome of growth, namely the maximum intensity, the growth time, and the meridional and zonal rate of propagation of the storm from genesis to maximum intensity (Section 2.2). Tracking all cyclones and anticyclones between the years 1940 and 2023 results in approximately 100,000 cyclones and 50,000 anticyclones. An in-depth discussion of the data appears in Section S3 in Supporting Information S1.

The model consists of multiple convolutional layers, each followed by max-pooling to reduce dimensionality, thus performing feature extraction. The resulting features then pass through two dense layers to regress on the storm properties. Additionally, the CNN was compared to a dense neural network (DNN) (no feature extraction) and a random forest (Breiman, 2001), implemented via `MLPRegressor` and `RandomForestRegressor` from scikit-learn (Pedregosa et al., 2011). Further details on the model architecture, hyperparameters, and this comparison can be found in Section S4 in Supporting Information S1.

3. Results

3.1. To What Extent Does the Mean Flow Set the Seasonal Storm Activity?

Seasonal storm activity becomes largely independent of SV because the long averaging period removes variability on the synoptic timescales. Consequently, if the mean atmospheric state captures most of the CF information, it should explain much of the variability in seasonal storm activity. To test this, the skill of a model in predicting EKE maps using only mean-flow fields is evaluated (Section 2.3). A comparison of an EKE snapshot from mid-November 2012, the corresponding model prediction, and the mid-November climatology (Figures 1b–1d) shows that the model captures key features, including the EKE "hot spots" along the Northern Hemisphere Atlantic and Pacific storm tracks, as well as many smaller-scale patterns linked to interannual variability. The proportion of overall EKE variability explained by the mean flow is equivalent to the R^2 of the model, and can be calculated based on the test set using:

$$R^2 = 1 - \frac{\sum \left(y_i - y_{\text{pred}}\right)^2}{\sum \left(y_i - \bar{y}\right)^2}, \tag{2}$$

where y_i and y_{pred} are the true and predicted EKE at each grid point over time (test set), and $\bar{y}$ is the overall mean EKE. As shown in Figure 1e, the model achieves R^2 values above 90% in most regions (shading), especially in regions of high climatological storm activity (contours). The model's main limitation is predicting EKE variability on the poleward flanks of the storm tracks. Overall, about 93% of the total EKE variability is explained. These results confirm that the mean flow contains the core CF information essential for determining the seasonally averaged storm activity, and that the averaging removes the dependence on synoptic conditions.

Shortening the averaging window for EKE reduces the model's predictive skill. However, as long as the window remains longer than the synoptic scale (roughly 10 days), the model still explains above 50% of the variability (Figure S3 in Supporting Information S1). Hence, the mean flow dominates storm-activity variability up to the scale of a single synoptic cycle. Moreover, model performance is relatively insensitive to which atmospheric

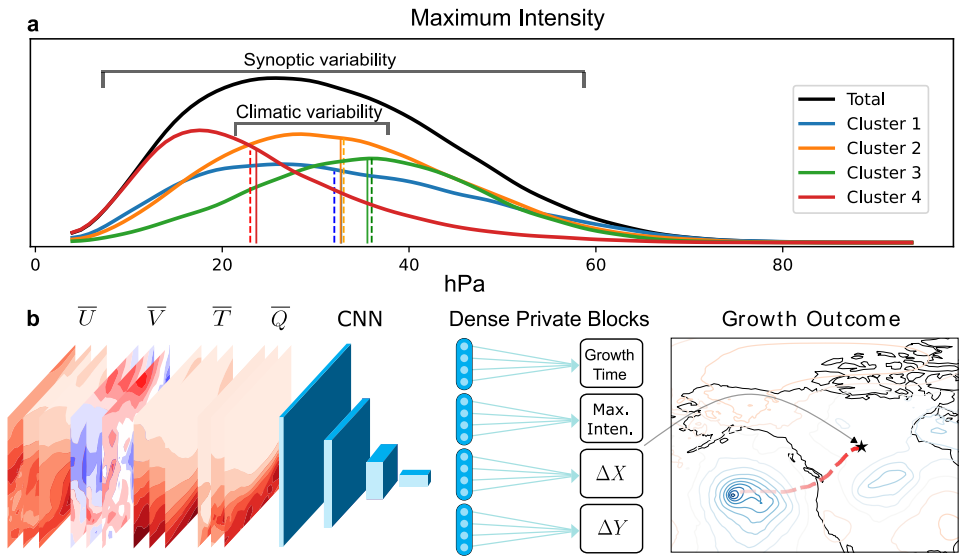

Figure 2. (a) The overall distribution of storms' maximum intensity (hPa, black curve), along with the corresponding distributions for four characteristic mean-flow conditions identified using K-means clustering. Solid and dashed vertical lines indicate the mean of each distribution and the model's mean prediction, respectively. The intensity distributions are smoothed using a cubic Hermite spline. (b) Illustration of the single-storm machine-learning model: the three-dimensional mean flow, temperature, and humidity at genesis, extracted within a composite box centered on the storm, is passed through a Convolutional Neural Network for feature extraction, and the model then predicts the storm's intensity growth and trajectory based on these extracted features.

variables are provided (Figure S4 in Supporting Information S1), with a single variable alone accounting for over 90% of the variance. This reflects how temporal averaging enforces consistency among mean-flow variables. For the dry variables, thermal wind balance provides a quantitative link between the mean temperature and wind profiles. The consistency with mean atmospheric water content can be understood qualitatively: atmospheric dynamics regulate the injection, removal, and distribution of water vapor, which then feeds back diabatically, resulting in tightly coupled climatologies. Repeating the analysis for the normalized SLP variance ($\overline{\mathrm{SLP}'^2}/\sin\phi$, Sanders & Gyakum, 1980), another common measure of storm activity, still yields high performance (82%), though marginally reduced, likely due to its sensitivity to variability throughout the atmospheric column.

3.2. To What Extent Does the Mean Flow Set the Growth of Individual Storms?

While the mean flow is largely consistent with the seasonally averaged storm activity, individual storms are also influenced by SV. For the following discussion, consider a flow X which is decomposed into a mean flow $\overline{X}$ and deviation X' such that $X = \overline{X} + X'$. To quantify the relative importance of the mean flow, a model is constructed to predict storm growth based solely on $\overline{X}$, as defined in Section 2.4. Because $\overline{X}$ encapsulates most of the relevant CF information for seasonal activity storm (Section 3.1), it is expected to provide an effective representation of CF's influence on individual storm dynamics. Meanwhile, SV is captured by the remainder of the atmospheric initial state, X'. Since storm dynamics also depend on X', there is a range of possible growth outcomes for any given $\overline{X}$ (Mana & Zanna, 2014). Consequently, a model that relies only on $\overline{X}$, cannot distinguish among these different outcomes. Instead, with a mean square error loss, it learns the single best-fit prediction for the observed distribution of outcomes, that is, the mean of that distribution (DelSole & Tippett, 2022). If $\overline{X}$ strongly controls storm growth variability, then holding $\overline{X}$ fixed produces only a narrow range of possible storm outcomes. Therefore, different values of $\overline{X}$ lead to clearly distinct outcome ranges, so a model that relies only on the mean flow performs well and has low error. On the other hand, if internal variability dominates, then even when $\overline{X}$ is fixed, the storm can evolve in many different ways. Then, each $\overline{X}$ corresponds to a broad spread of outcomes, which reduces the predictive power of a mean-flow-only model and results in higher error.

To illustrate this concept, the distribution of maximum storm intensities under different mean-flow conditions is approximated by clustering storms into four groups using K-means clustering applied to $\overline{X}$ (Figure 2a). The

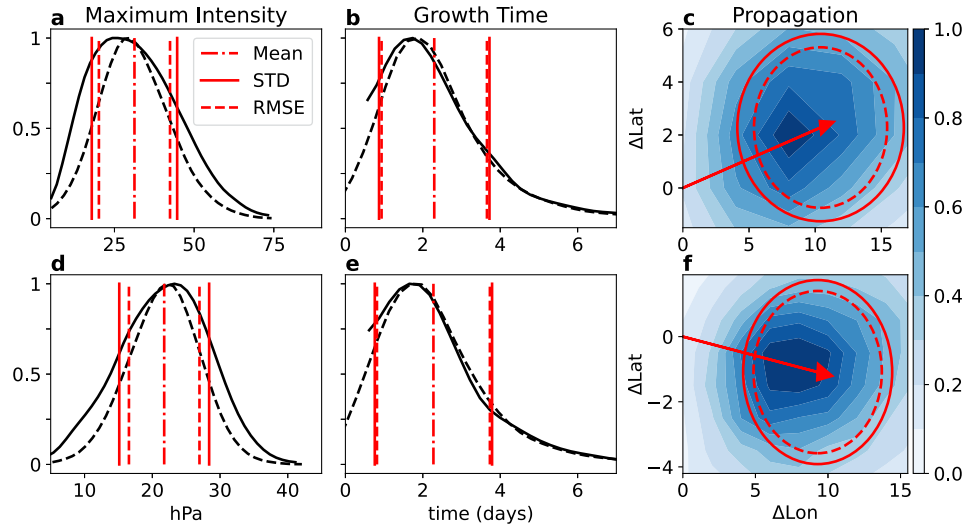

Figure 3. (a) Distribution of cyclones' maximum intensity (hPa, black curve), overlaid with the distribution of the model residual ($y - y_{\text{pred}}$, black dashed). The red dotted-solid line marks the mean, the red solid line marks the standard deviation (STD) of the distribution, and the red dashed line marks the model root mean square error (RMSE), which is the STD of the dashed residual curve. The residual distribution is shifted so that it has the same mean as the overall distribution. (b) Same as (a) but for growth time (days). (c) Two-dimensional distribution (color) of the zonal and meridional rate of propagation (degrees day^{-1}, abscissa, and ordinate respectively) from genesis to maximum intensity, along with the average propagation vector (red arrow), the STD (red solid ellipse), and the model RMSE (red dashed ellipse). The ellipse axes show the STD (RMSE) of the data (model) along each axis. (d–f) Same as (a–c) but for anticyclones.

resulting distributions are distinct, indicating that even coarse sorting by mean flow yields differences in growth outcomes. However, the within-cluster spread, approximately the SV, is large relative to the differences between the cluster means, reflecting variability associated with CF, hinting that internal variability dominates the overall dynamics. To go beyond this qualitative demonstration, a neural network is trained to learn the mapping between $\overline{X}$ and the expected storm growth (Figure 2b, see Section 2.4 for details). The network's predictions closely match the average maximum intensity observed within each cluster (Figure 2a, solid vs. dashed vertical lines). The model's mean square error, normalized by the total variance in storm intensity, then provides a quantitative estimate of the contribution of SV to storm growth variability. One minus this value gives the contribution of climatic variability, and also corresponds to the model's R^2.

Figure 3 compares the single-storm model's residual distribution against the overall distribution to illustrate the relative contributions of mean flow and SV. As indicated by the similar widths of the residual (dashed lines) and the original distribution (solid lines), most of the variability in individual storm properties cannot be explained by the mean flow. Quantitatively, for cyclones (anticyclones), the climatic variability accounts for only about 30% (38%) of the maximum intensity variability (Figures 3a and 3d), 7% (7%) of the growth-time variability (Figures 3b and 3e), 34% (25%) of the zonal propagation rate variability, and 25% (23%) of the meridional propagation rate variability (Figures 3c and 3f). The low climatic variability values show that most variability among storms on Earth arises from SV rather than from CF.

A series of sensitivity tests confirms the robustness of our single-storm model results. First, using only a DNN or a non-parametric random forest regressor yields nearly identical performance (Table S1 in Supporting Information S1). Second, training the model on at least 20,000 samples appears sufficient for convergence (Figure S5 in Supporting Information S1). Finally, the model's predictive skill increases significantly only when the averaging window $\overline{X}$ is shorter than about 10 days, an interval that begins to capture more SV (Figure S6).

3.3. To What Extent Do Long-Term Climate Trends Affect Storm Growth?

Due to anthropogenic forcing, the mean climate has significantly changed over the last decades (Forster et al., 2021; Vallis et al., 2015; Woollings et al., 2023). In this section, the portion of single-storm variability attributable to the long-term trends in the mean flow is investigated. This is achieved by comparing the

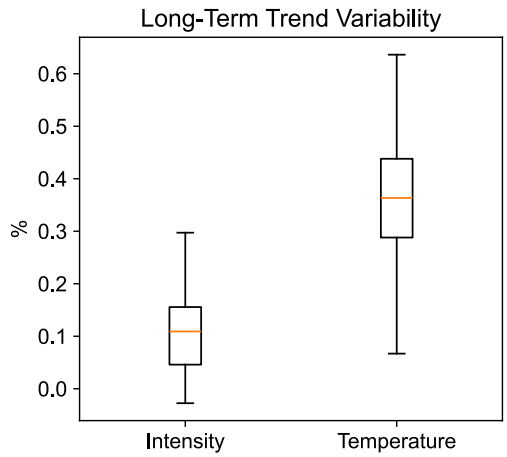

Figure 4. Box-and-whisker plots of the contribution of long-term trends to variability (%) for maximum intensity (Intensity) and temperature anomaly (Temperature). The box spans the interquartile range (IQR, Q3 minus Q1), the whiskers extend to the most extreme data points within 1.5 IQR, and the line inside the box marks the median.

predictability found in Section 3.2 to a modified test set in which any long-term trend is "scrambled," enabling a distinction between the predictability associated with long-term signals and other climate-driven variability (e.g., seasonal). Following prior studies (e.g., Woollings et al., 2023), the trend at each grid box is determined by linearly regressing mean flow on the year for each date. A modified test set is then created by removing the correct trend and adding the trend from a random year, thus preserving seasonal and interannual variability while eliminating the long-term signal. Finally, the performance (Section 2.4) on this modified data set is compared with that on the original test set, and the drop in skill is attributed to the long-term trend. In this section, only the years 1980–2023 are used, in order to focus on a period where the trend is largely due to anthropogenic effects (as can be assessed qualitatively from the global mean surface temperature trend, Forster et al. (2021)), and to reduce biases related to data availability (Soci et al., 2024). To estimate the uncertainty, the model is trained and tested 50 times, with different storms assigned to the training, validation, and testing sets each time.

Based on the method presented above, the long-term trend in the mean flow explains approximately 0.10(±0.02)% of cyclone intensity variability (Figure 4, error is defined as the 90% confidence interval). An important distinction is that this variability measure represents the average fraction of variance explained by the linear trend over 1980–2023, rather than the more standard comparison between historical and forced eras (e.g., 1980 vs. 2023). A linear trend distributes the total change gradually across all years, whereas a two-era comparison treats it as a single step, yielding more variance. However, a step change cannot be computed directly with the method above, since individual years contain too few storms to conduct the analysis. However, assuming a linear trend in the storm's response, the ratio between the variability associated with the linear trend and that obtained from a direct inter-era comparison can be analytically estimated to be 3 (see Section S5 in Supporting Information S1). Finally, normalizing by the global mean surface temperature change between 1980 and 2023 (defined in Section 2.1), the fraction of intensity variability that would be explained by climate change per degree of warming (assuming a linear response) is estimated to be $f_I = 0.36(\pm 0.08)\%/C^\circ$ (see Equation S7 in Text S5 in Supporting Information S1). Thus, accurately discerning such a weak signal poses a substantial challenge for attribution efforts, especially given the dominance of SV found in Section 3.2.

Nevertheless, these results do not imply that climate change is undetectable in the midlatitudes. As shown by many studies and supported here (Figure 1), temporally averaging storm activity diminishes the role of SV. Once the long-term signal rises above natural variability, its detection becomes feasible (Chemke & Coumou, 2024; Chemke & Yuval, 2026; Chemke et al., 2022; Priestley & Catto, 2022; Shaw et al., 2024). Furthermore, certain event attributes respond more directly to climate change, making them more amenable to attribution (Catto et al., 2019; Trenberth et al., 2015). For example, temperature anomalies accompanying cyclones (see Section 2.2) are expected to show a stronger climate-change signal due to robust warming. Indeed, re-training the model to predict temperature anomalies and scrambling the trend reveals that the fraction of variability explained by climate change is 0.35(±0.017)% (Figure 4). Following the same arguments as for the intensity response, the temperature response is $f_T = 1.22(\pm 0.23)\%/C^\circ$, more than three times higher than for cyclone intensity response. These findings underscore that, while attributing individual storm intensity changes to climate forcing remains difficult, examining variables more directly linked to a warming climate can offer a clearer attribution pathway.

4. Conclusions

Seasonal and interannual variations in atmospheric forcing create substantial variations in storm activity, which are commonly understood through eddy-mean flow interactions. However, storms are also influenced by the detailed atmospheric state in which they develop. This study quantifies the relative importance of the mean atmospheric state versus internal variability due to synoptic conditions for the activity of storms from both an averaged Eulerian perspective and an individual storm Lagrangian perspective.

From a climatic-Eulerian perspective, storm activity is almost entirely consistent with the mean flow, as more than 90% of the variation can be predicted from mean flow patterns using CNNs (Figure 1d). This demonstrates that even a 90-day average almost completely eliminates SV. However, from a Lagrangian perspective, focusing on individual weather events, only about 30% of the variability in storm behavior emerges from climate (Figure 3), indicating that individual storm dynamics are dominated by the detailed structure of initial conditions. This result quantifies how the balance between mean and eddy flow constrains individual storm dynamics, complementing recent research that demonstrates how climatic phenomena emerge from individual storm behavior (Federer et al., 2025; Hadas et al., 2023; Okajima et al., 2023; Schemm et al., 2021; Tamarin & Kaspi, 2017a, 2017b; Tamarin-Brodsky & Hadas, 2019). Future studies could employ explainable AI tools to identify which properties of the mean flow exhibit the strongest predictive power and to clarify which fields or aspects of storm activity can be skillfully predicted, thereby enabling comparison with theoretically based predictors currently in use.

Furthermore, this analysis reveals that long-term modulation in CF has limited effects on individual storm intensity. This is emphasized by our finding that only a small fraction of storm variability can be attributed to current long-term trends in the mean flow (Figure 4). This result highlights the challenge of attributing individual storm-related weather events to climate change, as even these trends might be affected by decadal variability, and underscores the importance of focusing attribution efforts on variables directly linked to climate change, such as positive temperature anomalies (Figure 4). These results might differ for extreme storms, as previous studies have shown that extreme events may respond differently to global warming than median storms (Chang, 2017). However, ERA-5-based results are too noisy due to insufficient data for tail distribution analysis (not shown). Future studies using larger data sets with stronger climate signals (e.g., CMIP6 SSP-8.5 scenarios) are needed to assess impacts on extreme individual storms and EKE seasons, adopting frameworks such as the one used in Palmer and Räisänen (2002).

Conflict of Interest

The authors declare no conflicts of interest relevant to this study.

Data Availability Statement

No new data sets were generated during the current study. A Python implementation of the models can be viewed in Hadas (2025). The three-dimensional atmospheric variables on pressure levels (e.g., zonal and meridional wind) are available from Copernicus through the data set "ERA-5 hourly data on pressure levels from 1940 to present" (Hersbach et al., 2023a). Sea level pressure data is available from Copernicus through the data set "ERA-5 hourly data on single levels from 1940 to present" (Hersbach et al., 2023b).

Acknowledgments
This research has been supported by the Azrieli fellowship and the Israeli Science Foundation (Grant 996/20). Computational work was carried out on the Weizmann HPC facility Chemfarm, supported in part by the Ben May Center for Chemical Theory and Computation. We thank Ido Aizenbud, Jonathan Kavitzki, Dotan Gazith, Gidi Yoffe, and Nimrod Gavriel for the meaningful discussion.

References

Bi, K., Xie, L., Zhang, H., Chen, X., Gu, X., & Tian, Q. (2023). Accurate medium-range global weather forecasting with 3D neural networks. *Nature*, *619*(7970), 533–538. https://doi.org/10.1038/s41586-023-06185-3

Breiman, L. (2001). Random forests. *Machine Learning*, *45*(1), 5–32. https://doi.org/10.1023/a:1010933404324

Catto, J. L., Ackerley, D., Booth, J. F., Champion, A. J., Colle, B. A., Pfahl, S., et al. (2019). The future of midlatitude cyclones. *Current Climate Change Reports*, *5*(4), 407–420. https://doi.org/10.1007/s40641-019-00149-4

Chang, E. K. M. (2017). Projected significant increase in the number of extreme extratropical cyclones in the southern hemisphere. *Journal of Climate*, *30*(13), 4915–4935. https://doi.org/10.1175/jcli-d-16-0553.1

Charney, J. G. (1947). The dynamics of long waves in a baroclinic westerly current. *Journal of Meteorology*, *4*(5), 136–162. https://doi.org/10.1175/1520-0469(1947)004<0136:tdolwi>2.0.co;2

Chemke, R., & Coumou, D. (2024). Human influence on the recent weakening of storm tracks in boreal summer. *npj Climate and Atmospheric Science*, *7*(1), 86. https://doi.org/10.1038/s41612-024-00640-2

Chemke, R., Ming, Y., & Yuval, J. (2022). The intensification of winter mid-latitude storm tracks in the southern hemisphere. *Nature Climate Change*, *12*(6), 553–557. https://doi.org/10.1038/s41558-022-01368-8

Chemke, R., & Yuval, J. (2026). Climate change shifts the North Pacific storm track polewards. *Nature*, *649*, 626–630. https://doi.org/10.1038/s41586-025-09895-y

DelSole, T., & Tippett, M. (2022). *Statistical methods for climate scientists*. Cambridge University Press. https://doi.org/10.1017/9781108659055

Eady, E. T. (1949). Long waves and cyclone waves. *Tellus*, *1*(3), 33–52. https://doi.org/10.3402/tellusa.v1i3.8507

Federer, M., Papritz, L., Sprenger, M., & Grams, C. M. (2025). Synoptic perspective on the conversion and maintenance of local available potential energy in extratropical cyclones. *Weather and Climate Dynamics*, *6*(1), 211–230. https://doi.org/10.5194/wcd-6-211-2025

Forster, P. M., Storelvmo, T., Armour, K., Collins, W., Dufresne, J.-L., Frame, D., et al. (2021). The Earth's energy budget, climate feedbacks, and climate sensitivity. In V. Masson-Delmotte, P. Zhai, A. Pirani, S. L. Connors, C. Péan, S. Berger, et al. (Eds.), *Climate change 2021: The*

physical science basis. Contribution of working group I to the sixth assessment report of the intergovernmental panel on climate change. Cambridge University Press. https://doi.org/10.1017/9781009157896

Ginesta, M., Yiou, P., Messori, G., & Faranda, D. (2023). A methodology for attributing severe extratropical cyclones to climate change based on reanalysis data: The case study of storm Alex 2020. *Climate Dynamics*, *61*(1), 229–253. https://doi.org/10.1007/s00382-022-06565-x

Guan, Y., Subel, A., Chattopadhyay, A., & Hassanzadeh, P. (2023). Learning physics-constrained subgrid-scale closures in the small-data regime for stable and accurate LES. *Physica D*, *443*, 133568. https://doi.org/10.1016/j.physd.2022.133568

Guillaumin, A. P., & Zanna, L. (2021). Stochastic-deep learning parameterization of ocean momentum forcing. *Journal of Advances in Modeling Earth Systems*, *13*(9), e2021MS002534. https://doi.org/10.1029/2021ms002534

Hadas, O. (2025). Models for climatological and single-storm analysis in "quantifying the influence of climate on storm activity using machine learning". *Zenodo*. https://doi.org/10.5281/zenodo.17150232

Hadas, O., Datseris, G., Blanco, J., Bony, S., Caballero, R., Stevens, B., & Kaspi, Y. (2023). The role of baroclinic activity in controlling Earth's albedo in the present and future climates. *Proceedings of the National Academy of Sciences of the United States of America*, *120*(5), e2208778120. https://doi.org/10.1073/pnas.2208778120

Hadas, O., & Kaspi, Y. (2025). A Lagrangian perspective on the growth of midlatitude storms. *AGU Advances*, *6*(3), e2024AV001555. https://doi.org/10.1029/2024av001555

Harnik, N., & Chang, E. K. M. (2004). The effects of variations in jet width on the growth of baroclinic waves: Implications for midwinter Pacific storm track variability. *Journal of the Atmospheric Sciences*, *61*(1), 23–40. https://doi.org/10.1175/1520-0469(2004)061<0023:teovij>2.0.co;2

Hersbach, H., Bell, B., Berrisford, P., Biavati, G., Horányi, A., Muñoz Sabater, J., et al. (2023a). ERA-5 hourly data on pressure levels from 1940 to present [Dataset]. *Copernicus Climate Change Service (C3S) Climate Data Store (CDS)*. https://doi.org/10.24381/cds.bd0915c6

Hersbach, H., Bell, B., Berrisford, P., Biavati, G., Horányi, A., Muñoz Sabater, J., et al. (2023b). ERA-5 hourly data on single levels from 1940 to present [Dataset]. *Copernicus Climate Change Service (C3S) Climate Data Store (CDS)*. https://doi.org/10.24381/cds.adbb2d47

Hersbach, H., Bell, B., Berrisford, P., Hirahara, S., Horányi, A., Muñoz-Sabater, J., et al. (2020). The ERA-5 global reanalysis. *Quarterly Journal of the Royal Meteorological Society*, *146*(730), 1999–2049. https://doi.org/10.1002/qj.3803

Hodges, K. (1995). Feature tracking on the unit sphere. *Monthly Weather Review*, *123*(12), 3458–3465. https://doi.org/10.1175/1520-0493(1995)123<3458:ftotus>2.0.co;2

Kochkov, D., Yuval, J., Langmore, I., Norgaard, P., Smith, J., Mooers, G., et al. (2024). Neural general circulation models for weather and climate. *Nature*, *632*(8027), 1060–1066. https://doi.org/10.1038/s41586-024-07744-y

Krizhevsky, A., Sutskever, I., & Hinton, G. E. (2012). Imagenet classification with deep convolutional neural networks. *Advances in Neural Information Processing Systems*, *25*.

Lam, R., Sanchez-Gonzalez, A., Willson, M., Wirnsberger, P., Fortunato, M., Alet, F., et al. (2023). Learning skillful medium-range global weather forecasting. *Science*, *382*(6677), 1416–1421. https://doi.org/10.1126/science.adi2336

Lenssen, N., Schmidt, G. A., Hendrickson, M., Jacobs, P., Menne, M. J., & Ruedy, R. (2024). A NASA GISTEMPv4 observational uncertainty ensemble. *Journal of Geophysical Research: Atmospheres*, *129*(17), e2023JD040179. https://doi.org/10.1029/2023jd040179

Mana, P. P., & Zanna, L. (2014). Toward a stochastic parameterization of ocean mesoscale eddies. *Ocean Modelling*, *79*, 1–20. https://doi.org/10.1016/j.ocemod.2014.04.002

Nakamura, H. (1992). Midwinter suppression of baroclinic wave activity in the Pacific. *Journal of the Atmospheric Sciences*, *49*(17), 1629–1642. https://doi.org/10.1175/1520-0469(1992)049<1629:msobwa>2.0.co;2

Okajima, S., Nakamura, H., & Kaspi, Y. (2023). Distinct roles of cyclones and anticyclones in setting the midwinter minimum of the North Pacific eddy activity: A Lagrangian perspective. *Journal of Climate*, *36*(14), 4793–4814. https://doi.org/10.1175/jcli-d-22-0474.1

Orlanski, I., & Chang, E. K. M. (1993). Ageostrophic geopotential fluxes in downstream and upstream development of baroclinic waves. *Journal of the Atmospheric Sciences*, *50*(2), 212–225. https://doi.org/10.1175/1520-0469(1993)050<0212:agfida>2.0.co;2

Orlanski, I., & Katzfey, J. (1991). The life cycle of a cyclone wave in the southern hemisphere. Part I: Eddy energy budget. *Journal of the Atmospheric Sciences*, *48*(17), 1972–1998. https://doi.org/10.1175/1520-0469(1991)048<1972:tlcoac>2.0.co;2

Palmer, T. N., & Räisänen, J. (2002). Quantifying the risk of extreme seasonal precipitation events in a changing climate. *Nature*, *415*(6871), 512–514. https://doi.org/10.1038/415512a

Pedregosa, F., Varoquaux, G., Gramfort, A., Michel, V., Thirion, B., Grisel, O., et al. (2011). Scikit-learn: Machine learning in Python. *Journal of Machine Learning Research*, *12*, 2825–2830.

Philip, S. Y., Kew, S. F., Van Oldenborgh, G. J., Anslow, F. S., Seneviratne, S. I., Vautard, R., et al. (2022). Rapid attribution analysis of the extraordinary heat wave on the Pacific coast of the US and Canada in June 2021. *Earth System Dynamics*, *13*(4), 1689–1713. https://doi.org/10.5194/esd-13-1689-2022

Phillips, N. A. (1954). Energy transformations and meridional circulations associated with simple baroclinic waves in a two level quasi-geostrophic model. *Tellus*, *6*(3), 273–286. https://doi.org/10.1111/j.2153-3490.1954.tb01123.x

Priestley, M. D., & Catto, J. L. (2022). Future changes in the extratropical storm tracks and cyclone intensity, wind speed, and structure. *Weather and Climate Dynamics*, *3*(1), 337–360. https://doi.org/10.5194/wcd-3-337-2022

Rivière, G., & Joly, A. (2006). Role of the low-frequency deformation field on the explosive growth of extratropical cyclones at the jet exit. Part I: Barotropic critical region. *Journal of the Atmospheric Sciences*, *63*(8), 1965–1981. https://doi.org/10.1175/JAS3729.1

Sanders, F., & Gyakum, J. R. (1980). Synoptic-dynamic climatology of the "bomb". *Monthly Weather Review*, *108*(10), 1589–1606. https://doi.org/10.1175/1520-0493(1980)108<1589:sdcot>2.0.co;2

Schemm, S., & Rivière, G. (2019). On the efficiency of baroclinic eddy growth and how it reduces the North Pacific storm-track intensity in midwinter. *Journal of Climate*, *32*(23), 8373–8398. https://doi.org/10.1175/JCLI-D-19-0115.1

Schemm, S., Wernli, H., & Binder, H. (2020). The North Pacific storm-track suppression explained from a cyclone life-cycle perspective. *Weather and Climate Dynamics Discussions*, 1–19. https://doi.org/10.5194/wcd-2-55-2021

Schemm, S., Wernli, H., & Binder, H. (2021). The storm-track suppression over the western North Pacific from a cyclone life-cycle perspective. *Weather and Climate Dynamics*, *2*(1), 55–69. https://doi.org/10.5194/wcd-2-55-2021

Shaw, T. A., Arblaster, J. M., Birner, T., Butler, A. H., Domeisen, D., Garfinkel, C. I., et al. (2024). Emerging climate change signals in atmospheric circulation. *AGU Advances*, *5*(6), e2024AV001297. https://doi.org/10.1029/2024av001297

Soci, C., Hersbach, H., Simmons, A., Poli, P., Bell, B., Berrisford, P., et al. (2024). The ERA-5 global reanalysis from 1940 to 2022. *Quarterly Journal of the Royal Meteorological Society*, *150*(764), 4014–4048. https://doi.org/10.1002/qj.4803

Tamarin, T., & Kaspi, Y. (2016). The poleward motion of extratropical cyclones from a potential vorticity tendency analysis. *Journal of the Atmospheric Sciences*, *73*(4), 1687–1707. https://doi.org/10.1175/jas-d-15-0168.1

Tamarin, T., & Kaspi, Y. (2017a). Mechanisms controlling the poleward deflection of midlatitude storm tracks. *Journal of the Atmospheric Sciences*, *73*, 553–572. https://doi.org/10.1175/JAS-D-16-0122.1

Tamarin, T., & Kaspi, Y. (2017b). The poleward shift of storm tracks under global warming: A Lagrangian perspective. *Geophysical Research Letters*, *44*(20), 10–666. https://doi.org/10.1002/2017gl073633

Tamarin-Brodsky, T., & Hadas, O. (2019). The asymmetry of vertical velocity in current and future climate. *Geophysical Research Letters*, *46*(1), 374–382. https://doi.org/10.1029/2018GL080363

Trenberth, K. E., Fasullo, J. T., & Shepherd, T. G. (2015). Attribution of climate extreme events. *Nature Climate Change*, *5*(8), 725–730. https://doi.org/10.1038/nclimate2657

Vallis, G. K. (2017). *Atmospheric and oceanic fluid dynamics*. Cambridge University Press. https://doi.org/10.1017/9781107588417

Vallis, G. K., Zurita-Gotor, P., Cairns, C., & Kidston, J. (2015). Response of the large-scale structure of the atmosphere to global warming. *Quarterly Journal of the Royal Meteorological Society*, *141*(690), 1479–1501. https://doi.org/10.1002/qj.2456

Woollings, T., Drouard, M., O'Reilly, C. H., Sexton, D. M., & McSweeney, C. (2023). Trends in the atmospheric jet streams are emerging in observations and could be linked to tropical warming. *Communications Earth & Environment*, *4*(1), 125. https://doi.org/10.1038/s43247-023-00792-8